International Journal of Minerals, Metallurgy and Materials
Volume 25, Number 12, December 2018, Page 1431
https://doi.org/10.1007/s12613-018-1697-1

Effect of melting temperature on microstructural evolutions, behavior and corrosion morphology of Hadfield austenitic manganese steel in the casting process

Masoud Sabzi[1)], *Sadegh Moeini Far*[2)], *and Saeid Mersagh Dezfuli*[3)]

1) Young Researchers and Elite Club, Dezful Branch, Islamic Azad University, Dezful 6461645165, Iran
2) Department of Mechanical Engineering, Islamic Azad University, Shushtar 6451741117, Iran
3) Department of Materials Science and Engineering, Islamic Azad University, Tehran 1477893855, Iran
(Received: 26 March 2018; revised: 15 May 2018; accepted: 16 May 2018)

Abstract: In this study, the effect of melting temperature on the microstructural evolutions, behavior, and corrosion morphology of Hadfield steel in the casting process is investigated. The mold was prepared by the sodium silicate/CO_2 method, using a blind riser, and then the desired molten steel was obtained using a coreless induction furnace. The casting was performed at melting temperatures of 1350, 1400, 1450, and 1500°C, and the cast blocks were immediately quenched in water. Optical microscopy was used to analyze the microstructure, and scanning electron microscopy (SEM) and X-ray diffractrometry (XRD) were used to analyze the corrosion morphology and phase formation in the microstructure, respectively. The corrosion behavior of the samples was analyzed using a potentiodynamic polarization test and electrochemical impedance spectroscopy (EIS) in 3.5wt% NaCl. The optical microscopy observations and XRD patterns show that the increase in melting temperature led to a decrease of carbides and an increase in the austenite grain size in the Hadfield steel microstructure. The corrosion tests results show that with increasing melting temperature in the casting process, Hadfield steel shows a higher corrosion resistance. The SEM images of the corrosion morphologies show that the reduction of melting temperature in the Hadfield steel casting process induced micro-galvanic corrosion conditions.

Keywords: Hadfield steel; casting process; melting temperature; microstructural evolutions; corrosion behavior; corrosion morphology

1. Introduction

In 1882, Robert Hadfield developed the first austenitic manganese steel containing 1.2wt% carbon and 12wt% manganese [1–2]. Austenitic steels with high-manganese content are classified under high-alloy steels and the most famous is called Hadfield steel, which is widely applied in various industries such as the cement, mining, road construction, and railway industries because of its good flexibility, high workability, and excellent wear resistance [2–5]. This steel is an alloy of iron, carbon, and manganese, but can contain other alloying elements depending on its application. One of these elements is titanium. The use of titanium for refining the microstructure and increasing the hardness of the steel has shown promising results [6–7]. Titanium addition results in the formation of stable carbides, which improve the hardness and wear resistance of Hadfield steel; however, these stable titanium carbides also reduce its toughness [8–9]. Sirvastava *et al.* [10] reported that with increase in the amounts of titanium carbides, the corrosion resistance of the Hadfield-TiC composite steel also decreases.

Over the past few decades, extensive research has been carried out on this steel, focused on increasing yield stress, increasing wear resistance, improving machining properties, grain refinement, and microstructural modification. Meanwhile, researchers have also aimed to achieve fine-grained homogeneous structures and investigate its effect on the mechanical properties of the steel. It has been reported that the use of elements such as boron, titanium, and vanadium as nuclei in this type of steel can also increase its wear re-

Corresponding author: Masoud Sabzi E-mail: mas.metallurg88@gmail.com

sistance while reducing grain size [11–14]. Hofer *et al.* [15] examined three types of austenitic manganese steel containing 12wt%, 16wt% and 22wt% Mn, and reported that 22wt% Mn steel gives the highest yield strength, and the 16wt% Mn steel shows better workability than the 12wt% Mn steel. The use of different percentages of chrome also increases the yield strength and results in a hard austenitic matrix [16–18].

For Hadfield austenitic manganese steel (HAMnS), excluding groups containing vanadium, chrome, and molybdenum, the ideal microstructure is a full austenitic and single-phase structure. In casting parts which are not heat-treated, the microstructures of the castings consist of austenitic matrix and carbide phases. The presence of carbide phase is due to the removal of carbon from the austenite phase during cooling. Carbides are commonly found at grain boundaries and inside the grains [19–22]. Because of the high-carbon content of HAMnS, its structure during casting comprises austenite grains and grain boundary precipitates, which results in brittleness unfit for application. This can be prevented by subjecting the steel to direct quenching in water after the casting process, as this removes the boundary carbides [20–24]. Hosseini *et al.* [25–26] reported that cooling Hadfield steel in a salt water solution after austenitizing heat treatment can prevent the formation of grain boundary carbide precipitates in the high-carbon steel microstructure.

Basically, the casting of Hadfield steel parts is similar to that of other steel parts and the risers are designed such that directional solidification is obtained. The design of the sprue, main gate, and sub-gate should be such that melts are quickly poured into the mold. Studies have shown that the presence of a high amount of carbon and cementite in Hadfield steel microstructure as well as low heat conductivity may result in cracking in some parts and when cutting risers. For thick parts with large risers, it is recommended to cut the rises after heat treatment. The alternative is to use narrow-necked risers which are made of sheared cores. Hadfield steel can be casted in a variety of green and dry sands. Hadfield steel melt strongly reacts with acidic refractory materials and causes severe sand burning. The molten steel also reacts with the SiO_2 of silicate sand and creates the eutectic composition of $MnSiO_3$ + Mn_2SiO_4, which has a melting point of below 1250°C, and causes severe sand burning [18–25].

Undoubtedly, the presence of alloying elements and the steelmaking process have a great influence on the mechanical and corrosion properties of steels. Toor [27] showed that by reducing the amount of manganese and increasing the solution annealing temperature, the corrosion resistance of austenitic steels increases.

As can be deduced from above, less attention has been given to the corrosion behavior of Hadfield steels compared to the mechanical properties. Given that the destruction of the parts made of HAMnS is very costly in terms of service, this study evaluates the effect of the melting temperature during casting on the microstructural evolution, corrosion behavior, and corrosion potential of Hadfield steel to the micro-galvanic local corrosion, which has not been the subject of previous studies.

2. Experimental

The steel used in this study is ASTM A-128 HAMnS. To produce this alloy, four Y-shaped models made of aluminum were provided and then molded by sodium silicate/CO_2 method using a blind riser. Melting temperatures of 1350, 1400, 1450, and 1500°C were used for the casting, and the desired molten steel was obtained using a coreless induction furnace. After casting, the casts were quenched in cold pure water. Chemical analyses of the samples were controlled by a spark emission spectrometer (Foundry Master Optimum, Germany), and the related data are reported in Table 1.

Table 1. Chemical compositions of the used steel wt%

Sample	C	Mn	Si	P	Fe
ASTM A-128	1–1.4	10–14	1 Max	0.07 Max	Bal.
Casted steel	1.24	11.28	0.410	0.020	Bal.

To evaluate the microstructure of the castings, the samples were polished by different sandpapers and etched with 2vol% nital solution, and their microstructure was studied by an optical microscope. The metallographic test was carried out according to ASTM E112. The grain sizes of the four samples were measured by an image analyzer software, and the amounts of the carbides were determined by Image J software. X-ray diffractrometry (XRD) was also used to study the effect of melting temperature (1350 and 1500°C) on the formed phases in the Hadfield steel microstructure.

To prepare the corrosion test samples, cylindrical samples with 10 mm diameter and 30 mm height were cut from the four casted samples and were polished to obtain uncontaminated surfaces. Then around 1 cm^2 area of each polished sample was exposed to 3.5wt% NaCl solution and the remaining surface was coated. In this stage, one side of the prepared sample was poured into the NaCl solution and the other side was clamped to a measurement device. To evaluate the corrosion behavior of the Hadfield steel samples in

3.5wt% NaCl solution, each sample was immersed for half hour at open circuit potential to reach the stable state. First, electrochemical impedance spectroscopy (EIS) analysis was performed at open circuit potential using an amplitude of 10 mV in a frequency of −10 mHz–100 kHz. Then potentiodynamic polarization analysis was performed in −500 mV–1000 mV versus open circuit potential, with a scanning rate of 0.001 V/s. Then, using the gradient of the Tafel graph in the anodic and cathodic regions as well as Nova software, the corrosion current intensity, corrosion resistance, and corrosion rate of all four casting samples were calculated.

The corrosion tests were performed using a three-electrode standard cell, with Ag/AgCl as reference electrode, platinum as auxiliary electrode, and steel samples as working electrode, and the cell was connected to a potentiostat-galvanostat machine (Autolab Galvanostat PGStat 302N). The two corrosion tests were performed at 25°C and were repeated three times to ensure accurate results. After the potentiodynamic polarization test, scanning electron microscope (SEM) images of the surfaces with the highest and lowest corrosion resistances were obtained and the corrosion morphologies of the Hadfield austenitic steels were analyzed.

3. Results and discussion

3.1. Microstructural observations and phase analysis

After casting the four HAMnS samples at different temperatures and quenching in pure water, the microstructures of all four samples contained an austenitic matrix and different amounts of carbides, as shown by an optical microscope (Fig. 1). The presence of carbide is due to the presence of high-carbon content and carbidizing elements such as manganese and iron, and the presence of austenitic matrix is due to the presence of carbon and high-manganese content. Several researchers [28] have reported that with the increase in the manganese content of Fe–Mn alloys, the martensite start temperature reduces considerably, so that in a high-manganese alloy, a completely austenitic matrix can be observed. The images show that with increasing melting temperature, the size of the austenite grains increases and the amounts of carbidizing particles reduces. Because of the increase in melting temperature, the preferred nucleation sites melt and will be removed. As a result, with the increase of melting temperature, the preferred nucleation sites are reduced, fewer austenite grains are formed, and the numbers of grain boundaries and carbides decrease, as shown in the metallographic images. The measured grain sizes by an image analyzer software shows that an increase of 150°C in the melting temperature of the HAMnS casting process results in a double increase of the austenite grains sizes in the Hadfield steel microstructure. The amounts of carbide particles of four samples were measured by Image J software, and as shown in Table 2, the amount of carbide decreases with an increase of melting temperature.

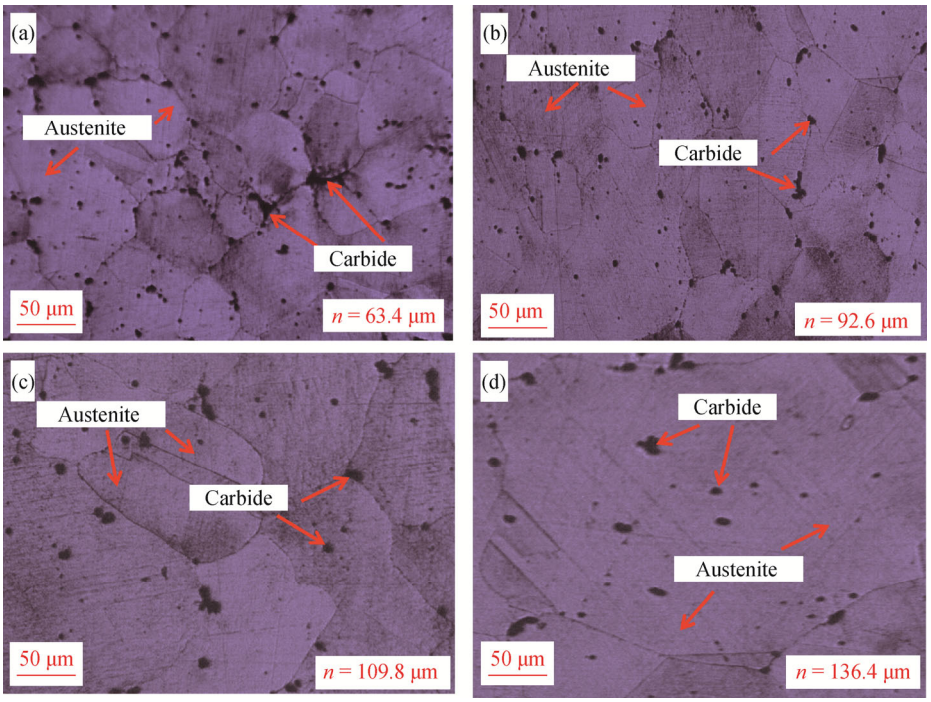

Fig. 1. Optical metallographic images at 100x magnification for Hadfield steel casted with melting temperatures of (a) 1500, (b) 1450, (c) 1400, and (d) 1350°C, respectively.

Table 2. Determination of carbide distribution in different samples using Image J software

Melting temperature / °C	Amount of carbide / %	Standard deviation / %
1350	17.03	0.78
1400	12.07	0.39
1450	6.28	0.32
1500	5.26	0.14

The formed precipitates in the casting samples with melting temperatures of 1350 and 1500°C were studied by XRD. The carbides of the two samples are of type Mn_3C, and the dominant phase (matrix phase) is austenite (Fig. 2) [4–9]. Moreover, it can be observed from the X-ray diffraction patterns that the increase in the intensity of Mn_3C is higher in the casting samples with 1350°C melting temperature compared to those with 1500°C melting temperature, which is consistent with microscopic observations and measured precipitates by the software.

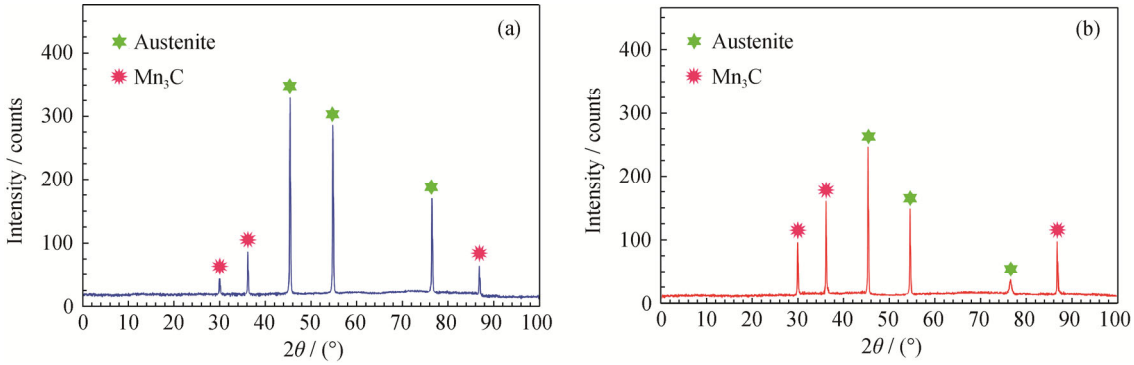

Fig. 2. X-ray diffraction patterns obtained for the casting samples with melting temperature of (a) 1500°C and (b) 1350°C.

3.2. Potentiodynamic polarization test

Of the four samples, the casting sample with melting temperature of 1500°C has the highest corrosion resistance, highest corrosion potential, and stable corrosion current and corrosion rate (Fig. 3 and Table 3); this is because of the lower amounts of carbides and grain boundaries. I_{Corr} denotes the corrosion current intensity, and R_p denotes the corrosion resistance. The sample with melting temperature of 1350°C has the weakest corrosion resistance because of the presence of more carbide particles and higher grain boundaries. In Hadfield manganese steel, the composition of carbide particles show a higher behavior compared to the austenitic matrix [29–30]. However, when high amounts of carbides are formed in the sample with low melting temperature, the corrosion intensifies for the following two reasons [29–31]: (1) The casting samples with low melting temperatures have lower grain sizes because of the higher carbide content. As a result, in these samples, the number of grain boundaries is higher than that of low melting temperatures. The grain boundaries are high energy sites which are chemically more active and prone to corrosion. (2) When high carbide particles are placed next to the active matrix, an electrochemical couple forms and causes lower corrosion resistance.

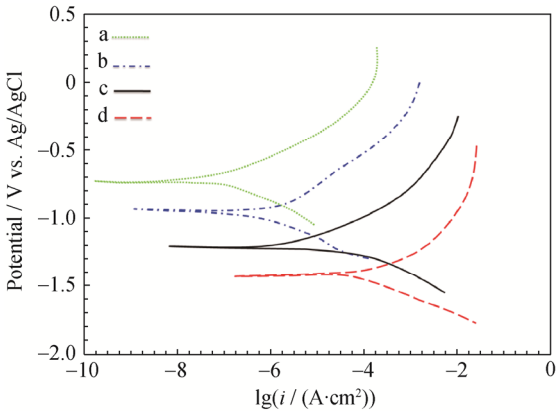

Fig. 3. Potentiodynamic polarization test graphs with at least three times repeatability for the casting samples with melting temperatures of (a) 1500, (b) 1450, (c) 1400, and (d) 1350°C, respectively.

Table 3. Potentiodynamic polarization test results with at least three times repeatability

Melting temperature / °C	I_{corr} / (μA·cm^{-2})	E_{corr} / V	R_p / (Ω·cm^2)	Cr / (mm·a^{-1})
1350	24714 ± 4	−1.481 ± 0.007	35.1 ± 0.3	3.2627 ± 0.22
1400	4517 ± 5	−1.228 ± 0.011	70.8 ± 0.2	2.4307 ± 0.16
1450	2469 ± 3	−0.996 ± 0.008	124.2 ± 0.3	1.6314 ± 0.18
1500	651 ± 3	−0.693 ±0.009	199.1 ± 0.5	0.7051 ± 0.21

Note: E_{corr} expresses the corrosion potential and Cr indicates the corrosion rate.

Briefly, the potentiodynamic polarization test results show that the increasing melting temperature from 1350 to 1500°C in HAMnS casting leads to better corrosion resistance. The potentiodynamic polarization test results are consistent with those of Srivastava *et al.* [10]. They reported that titanium carbide particles cause lower corrosion resistance of the Hadfield-TiC composite.

3.3. Electrochemical impedance spectroscopy test

The sample with melting temperature of 1500°C has more actual impedance resistance compared to the other samples (Fig. 4). The actual impedance resistance for the samples with melting temperatures of 1500, 1450, 1400, and 1350°C are 332, 272, 217, and 136 Ω·cm^2, respectively. The EIS test results directly correspond with the microstructural evolutions.

By reducing the melting temperature in the HAMnS casting process, the amounts of carbide precipitates and grain boundaries increases, consequently creating the conditions for corrosion intensification. The diameters of the semicircles in the Nyquist diagrams represent the polarization resistance of the samples [32–34]. Hence, comparing the semicircles, the sample with melting temperature of 1500°C (lower amounts of carbide and grain boundaries) has more polarization resistance than the other samples. The corrosion resistance results of EIS test also consist of the potentiodynamic polarization test results.

The equivalent circuit consists of a solution resistance, constant phase element, and charge transfer resistance (Fig. 5) [35], and the impedance resistance increases because of the increase of melting temperature from 1350 to 1500°C during the HAMnS casting (Table 4). Where R_s is the solution resistance, C_{PE} is the constant phase element (capacity), and R_{ct} is the charge transfer resistance. Also, n represents the capacitive behavior of the sample surface.

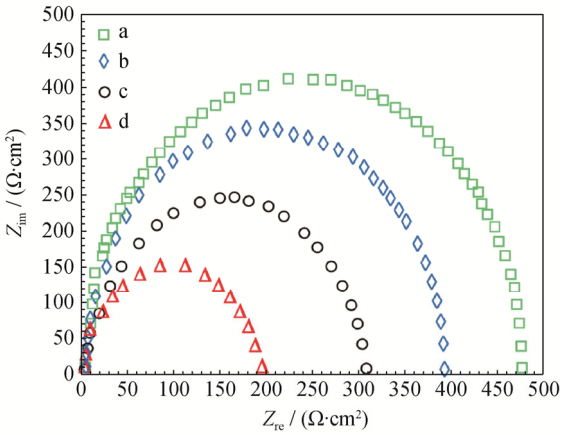

Fig. 4. Nyquist diagram of electrochemical impedance spectroscopy test with at least three times repeatability for the casting samples with melting temperatures of (a) 1500, (b) 1450, (c) 1400, and (d) 1350°C, respectively.

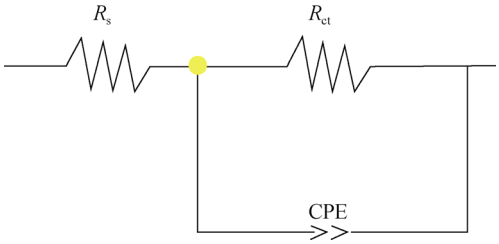

Fig. 5. Equivalent circuit used for the calculation of electrochemical impedance spectroscopy test parameters.

Table 4. Electrochemical impedance spectroscopy test results with at least three times repeatability

Melting temperature / °C	R_s / (Ω·cm^2)	C_{PE} / (μF·cm^{-2}·s^{n-1})	R_{ct} / (Ω·cm^2)	n
1350	0.0202	21.5204	198.1 ± 0.1	0.80 ± 0.2
1400	0.0204	27.6316	308.2 ± 0.2	0.84 ± 0.1
1450	0.0209	33.6197	395.5 ± 0.3	0.89 ± 0.2
1500	0.0206	41.3110	477.9 ± 0.3	0.96 ± 0.2

The Bode and Bode-phase graphs of the EIS measurements are reported in Figs. 6(a) and 6(b), respectively. Principally, a Bode graph for an alloy with appropriate protective properties is a straight line with the gradient (−1). However, with the movement of corrosive ions (e.g., Cl^- ions) and oxygen into the surface layers of the alloy, the slope of the Bode graph changes, and then corrosion begins in the electrolyte/alloy interface. Thus, the protective behavior of an alloy in a simulated corrosive setting can be examined using the distortion of Bode graph gradient [36–38].

In Fig. 6(a), the Bode graph of the EIS measurements is shown for Hadfield steel casted at various temperatures. From the Bode graph, two significant points can be inferred: (1) All the Bode graphs for Hadfield steel casted at different temperatures have negative slopes. The existence of only a negative slope in the Bode graph indicates that there is only one constant phase element in the impedance graphs of the Hadfield steel [37–38]. Overall, the Bode graphs shown in Fig. 6(a) corresponds with the designed equivalent circuit and can be used for extracting the parameters of the impedance of a Hadfield steel casted at various temperatures. (2) As is seen in the Bode graphs, with increase in the melting

temperature from 1350 to 1500°C in the HAMnS casting process, the steel impedance resistance increases. The similarity of Bode graphs to the Nyquist diagrams indicates that the increase of melting temperature improves the corrosion resistance of HAMnS.

There is only one peak in the Bode-phase graphs of the Hadfield steels casted at different temperatures (Fig. 6(b)), confirming the presence of a constant phase element in the results of impedance samples studied, and the Hadfield steel casting of 1500°C has the highest peak. The higher the peak in Bode-phase, the higher the corrosion resistance of the alloy and the protective properties of the Hadfield steel [36–40]. The highest peak in −50° is related to Hadfield steel casing at 1500°C. Overall, all the results obtained from electrochemical tests (Nyquist, Bode, and Bode-phase) coincide with each other.

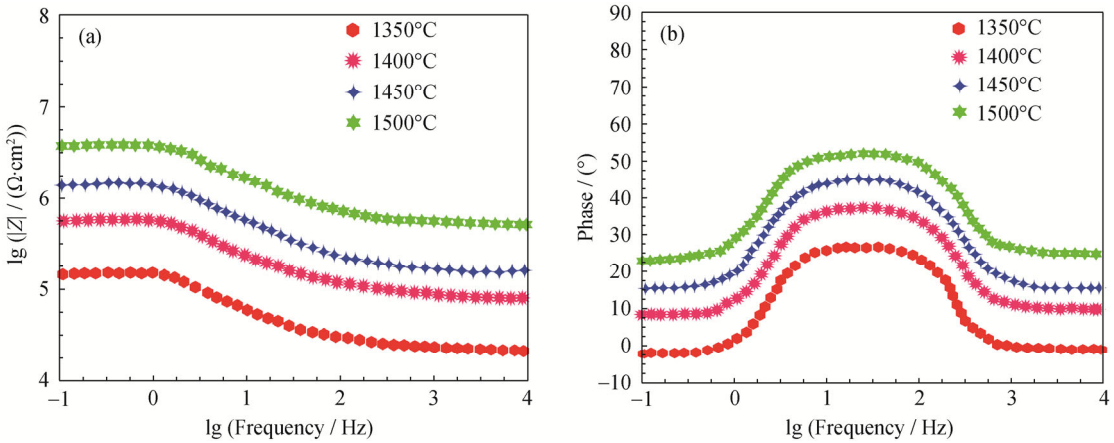

Fig. 6. Resulting from electrochemical impedance spectroscopy test with different melting temperatures: (a) Bode graph and (b) Bode-phase graph.

3.4. Corrosion morphology of the samples

To investigate the effect of the casting process melting temperature on the corrosion morphology of HAMnS, after potentiodynamic polarization tests, SEM images of the casted samples with melting temperatures of 1500 and 1350°C were obtained. In the corrosion surface of the casted sample with 1350°C melting temperature, there are some large porosities compared to that with 1500°C melting temperature (Fig. 7). This is because by decreasing the melting temperature, the amounts of carbide particles and grain boundaries in the microstructure increases, and the presence of high amounts of carbide particles contributes to the formation of micro-cells and intensifies the local micro-galvanic corrosion, with the carbide particles as the cathode and the austenite matrix as the anode [36–37]. In addition, the corrosion rate of the surface of two casted samples (the number and depth of cavities) is consistent with the obtained test results of corrosion resistance and corrosion rate. An evaluation of the corrosion surfaces showed that corrosion effects in the HAMnS were in the form of cavities, in which the number and depths of these cavities were reduced by increasing the melting temperature of the casting process.

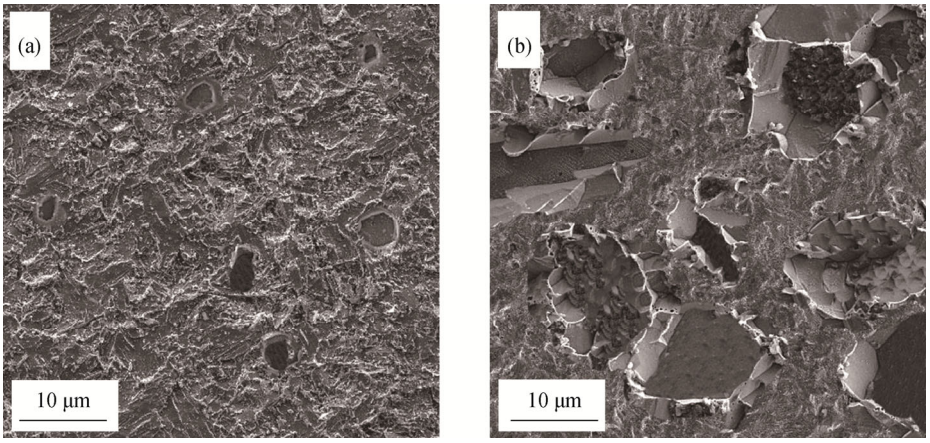

Fig. 7. SEM images after potentiodynamic polarization test from the corrosion surface of the casted samples with melting temperatures of (a) 1500°C and (b) 1350°C.

On the other hand, by comparing the corrosion morphology of the samples with melting temperatures of 1350 and 1500°C, it was observed that the surface of the sample with melting temperature of 1500°C experienced uniform and less corrosion which is consistent with the potentiodynamic polarization tests results. Furthermore, SEM images indicate that in addition to weakening the HAMnS corrosion resistance, decreasing the melting temperature from 1500 to 1350°C changes the corrosion mechanism from a uniform state to local micro-galvanic corrosion.

4. Conclusions

(1) The optical microscope observations show that increasing the melting temperature in the HAMnS casting process leads to an increase in the size of the austenite grains and decrease in the carbides precipitates. In addition, for any melting temperature, the dominant phase in the microstructure (main phase) is austenite.

(2) The XRD analysis results indicate that in the HAMnS casted with different melting temperatures, the formed manganese carbides are of type Mn_3C, and increasing the melting temperature reduces the manganese carbides in the microstructure. Moreover, austenite is the dominant phase (matrix phase) in the casted samples for any melting temperature.

(3) Potentiodynamic polarization and EIS tests imply that the HAMnS corrosion resistance is reduced by decreasing the melting temperature. The reduction of melting temperature as well as an increase in the number of grain boundaries and high Mn_3C particles formation, besides austenitic matrix, provides the conditions for corrosion intensification and increased corrosion rate.

(4) Scanning electron microscope observations indicate that reduction of melting temperature in the casting process changes the HAMnS corrosion mechanism from a uniform state to local micro-galvanic state. This is because the low melting temperature can result in the formation of micro-galvanic cells (high carbide particles next to an active matrix).

References

[1] L. Ma, C. Huang, K. Dolman, X.H. Tang, J.J. Yang, Z. Shi, and Z.S. Liu, A method to calculate the bulk hardness of metal matrix composite using Hadfield steel reinforced with niobium carbide particles as an example, *Mech. Mater.*, 112(2017), p. 154.

[2] C. Chen, X.Y. Feng, B. Lv, Z.N. Yang, and F.C. Zhang, A study on aging carbide precipitation behavior of hadfield steel by dynamic elastic modulus, *Mater. Sci. Eng. A*, 677(2016), p. 446.

[3] D.V. Lychagin, A.V. Filippov, O.S. Novitskaia, Y.I. Chumlyakov, E.A. Kolubaev, and O.V. Sizova, Friction-induced slip band relief of -Hadfield steel single crystal oriented for multiple slip deformation, *Wear*, 374(2017), p. 5.

[4] C. Chen, F.C. Zhang, F. Wang, H. Liu, and B.D. Yu, Effect of N+Cr alloying on the microstructures and tensile properties of Hadfield steel, *Mater. Sci. Eng. A*, 679(2017), p. 95.

[5] S.F. Gnyusov, V.P. Rotshtein, A.E. Mayer, E.G. Astafurova, V.V. Rostov, A.V. Gunin, and G.G. Maier, Comparative study of shock-wave hardening and substructure evolution of 304L and Hadfield steels irradiated with a nanosecond relativistic high-current electron beam, *J. Alloys Compd.*, 714(2017), p. 232.

[6] J.T. Horng and K.T. Chiang, A grey and fuzzy algorithms integrated approach to the optimization of turning Hadfield steel with Al_2O_3/TiC mixed ceramic tool, *J. Mater. Process. Technol.*, 207(2008), No. 1-3, p. 89.

[7] I. Mejía, A.E. Salas-Reyes, J. Calvo, and J.M. Cabrera, Effect of Ti and B microadditions on the hot ductility behavior of a high-Mn austenitic Fe–23Mn–1.5Al–1.3Si–0.5C TWIP steel, *Mater. Sci. Eng. A*, 648(2015), p. 311.

[8] D. Siafakas, T. Matsushita, Å. Lauenstein, S. Ekero, and A.E.W. Jarfors, A particle population analysis in Ti- and Al-deoxidized Hadfield steels, *Int. J. Cast Met. Res.*, 31(2018), No. 3, p. 125.

[9] A.K. Srivastava and K. Das, *In-situ* synthesis and characterization of TiC-reinforced Hadfield manganese austenitic steel matrix composite, *ISIJ Int.*, 49(2009), No. 9, p. 1372.

[10] A.K. Srivastava, K. Das, and S.K. Toor, Corrosion behaviour of TiC-reinforced Hadfield manganese austenitic steel matrix *in-situ* composites, *Open J. Met*. 5(2015), No. 2, p. 11.

[11] X.Y. Feng, F.C. Zhang, Z.N. Yang, and M. Zhang, Wear behaviour of nanocrystallised Hadfield steel, *Wear*, 305(2013), No. 1-2, p. 299.

[12] G.S. Zhang, J.D. Xing, and Y.M. Gao, Impact wear resistance of WC/Hadfield steel composite and its interfacial characteristics. *Wear*, 260(2006), No. 7-8, p. 728.

[13] W.L. Yan, L. Fang, K. Sun, and Y.H. Xu, Effect of surface work hardening on wear behavior of Hadfield steel, *Mater. Sci. Eng. A*, 460(2007), p. 542.

[14] Y.N. Dastur and W.C. Leslie, Mechanism of work hardening in Hadfield manganese steel, *Metall. Trans. A*, 12(1981), No. 5, p. 749.

[15] S. Hofer, M. Hartl, G. Schestak, R. Schneider, E. Arenholz, and L. Samek, Comparison of austenitic high-Mn-steels with different Mn- and C-contents regarding their processing properties, *BHM Berg- Huttenmann. Monatsh.*, 156(2011), No. 3, p. 99.

[16] S.M. Anijdan, M. Sabzi, M. Ghobeiti-Hasab, and A. Roshan-Ghiyas, Optimization of spot welding process parameters in dissimilar joint of dual phase steel DP600 and AISI 304 stainless steel to achieve the highest level of shear-tensile

strength, *Mater. Sci. Eng. A*, 726(2018), p. 120.

[17] C. Iglesias, I.G. Solórzano, and B.J. Schulz, Effect of low nitrogen content on work hardening and microstructural evolution in Hadfield steel, *Mater Charact.*, 60(2009), No. 9, p. 971.

[18] T. Kıvak, Optimization of surface roughness and flank wear using the Taguchi method in milling of Hadfield steel with PVD and CVD coated inserts, *Measurement*, 50(2014), p. 19.

[19] E. Bayraktar, F.A. Khalid, and C. Levaillant, Deformation and fracture behaviour of high manganese austenitic steel, *J. Mater. Process. Technol.*, 147(2004), No. 2, p. 145.

[20] D. Canadinc, H. Sehitoglu, and H.J. Maier, The role of dense dislocation walls on the deformation response of aluminum alloyed Hadfield steel polycrystals, *Mater. Sci. Eng. A*, 454(2007), p. 662.

[21] S.H.M. Anijdan and M. Sabzi, The evolution of microstructure of an high Ni HSLA X100 forged steel slab by thermomechanical controlled processing, [in] *TMS Annual Meeting & Exhibition*, Cham, 2018, p. 145.

[22] I. Karaman, H. Sehitoglu, Y.I. Chumlyakov, H.J. Maier, and I.V. Kireeva, Extrinsic stacking faults and twinning in Hadfield manganese steel single crystals, *Scr. Mater.*, 44(2001), No. 2, p. 337.

[23] D. Canadinc, H. Sehitoglu, H.J. Maier, and Y.I. Chumlyakov, Strain hardening behavior of aluminum alloyed Hadfield steel single crystals, *Acta Mater.*, 53(2005), No. 6, p. 1831.

[24] M. Sabzi, A. Obeydavi, and S.H.M. Anijdan, The effect of joint shape geometry on the microstructural evolution, fracture toughness, and corrosion behavior of the welded joints of a Hadfield steel, *Mech. Adv. Mater. Struct.*, (2018), p. 1. https://doi.org/10.1080/15376494.2018.1430268.

[25] S. Hosseini and M.B. Limooei, Optimization of heat treatment to obtain desired mechanical properties of high carbon Hadfield steels, *World Appl. Sci. J.*, 15(2011), No. 10, p. 1421.

[26] S. Hosseini, M.B. Limooei, M.H. Zade, E. Askarnia, and Z. Asadi, Optimization of heat treatment due to austenising temperature, time and quenching solution in Hadfield steels, *Int. J. Chem. Mol. Nucl. Mater. Metall. Eng.*, 7(2013), No. 7, p. 582.

[27] I.U.H. Toor, Effect of Mn content and solution annealing temperature on the corrosion resistance of stainless steel alloys, *J. Chem*., 2014(2014), p. 1.

[28] Y.K. Lee and C.S. Choi, Driving force for γ→ε martensitic transformation and stacking fault energy of γ in Fe–Mn binary system, *Metall. Mater. Trans. A*, 31(2000), No. 2, p. 355.

[29] T.E. Abioye, P.K. Farayibi, D.G. McCartney, and A.T. Clare, Effect of carbide dissolution on the corrosion performance of tungsten carbide reinforced Inconel 625 wire laser coating, *J. Mater. Process. Technol.*, 231(2016), p. 89.

[30] S.H.M. Anijdan, M. Sabzi, M.R. Zadeh, and M. Farzam, The effect of electroless bath parameters and heat treatment on the properties of Ni–P and Ni–P–Cu composite coatings, *Mater. Res.*, 21(2018), No. 2, p. 1.

[31] J. Li, J.S. Wu, Z. Wang, S.Q. Zhang, X.G. Wu, Y.H. Huang, and X.G. Li, The effect of nanosized NbC precipitates on electrochemical corrosion behavior of high-strength low-alloy steel in 3.5% NaCl solution, *Int. J. Hydrogen Energy*, 42(2017), No. 34, p. 22175.

[32] J. Sanchez, J. Fullea, and C. Andrade, Corrosion-induced brittle failure in reinforcing steel, *Theor. Appl. Fract. Mech.*, 92(2017), p. 229.

[33] T.R. Tamilarasan, U. Sanjith, M.S. Shankar, and G. Rajagopal, Effect of reduced graphene oxide (rGO) on corrosion and erosion-corrosion behaviour of electroless Ni–P coatings, *Wear*, 390 (2017), p. 385.

[34] D.J. Blackwood, C.S. Lim, S.L.M. Teo, X.P. Hu, and J.J. Pang, Macrofouling induced localized corrosion of stainless steel in Singapore seawater, *Corros. Sci.*, 129(2017), p. 152.

[35] J.H. Hong, S.H. Lee, J.G. Kim, and J.B. Yoon, Corrosion behaviour of copper containing low alloy steels in sulphuric acid, *Corros. Sci.*, 54(2012), p. 174.

[36] R.Q. Hou, C.Q. Ye, C.D. Chen, S.G. Dong, M.Q. Lv, S. Zhang, J.S. Pan, G.L. Song, and C.J. Lin, Localized corrosion of binary Mg–Ca alloy in 0.9wt% sodium chloride solution, *Acta Metall. Sinica (Engl. Lett.)*, 29(2016), No. 1, p. 46.

[37] M.L.C. Lim, R.G. Kelly, and J.R. Scully, Overview of intergranular corrosion mechanisms, phenomenological observations, and modeling of AA5083, *Corros. Sci.*, 72(2016), No. 2, p. 198.

[38] M. Sabzi, S.H.M. Anijdan, and M. Asadian, The effect of substrate temperature on microstructural evolution and hardenability of tungsten carbide coating in hot filament chemical vapor deposition, *Int. J. Appl. Ceram. Technol.*, 15(2018), No. 6, p. 1350.

[39] S.M. Dezfuli and M. Sabzi, A study on the effect of presence of CeO_2 and benzotriazole on activation of self-healing mechanism in ZrO_2 ceramic-based coating, *Int. J. Appl. Ceram. Technol.*, 15(2018), No. 5, p. 1248.

[40] M. Sabzi, S.H.M. Anijdan, M.R. Zadeh, and M. Farzam, The effect of heat treatment on corrosion behaviour of Ni–P–3 gr/lit Cu nano-composite coating, *Can. Metall. Q.*, 57(2018), No. 3, p. 350.